IEEE Access
Multidisciplinary | Rapid Review | Open Access Journal

Received January 4, 2020, accepted January 21, 2020, date of publication January 29, 2020, date of current version February 6, 2020.

Digital Object Identifier 10.1109/ACCESS.2020.2970209

Dual-Band Bandpass Filter and Filtering Power Divider With Ultra-Wide Upper Stopband Using Hybrid Microstrip/DGS Dual-Resonance Cells

YUNBO RAO[1], (Student Member, IEEE), HUIZHEN JENNY QIAN[1], (Member, IEEE), BINGZHENG YANG[1], (Student Member, IEEE), ROBERTO GÓMEZ-GARCÍA[1,2], (Senior Member, IEEE), AND XUN LUO[1], (Senior Member, IEEE)

[1]State Key Laboratory of Electronic Thin Films and Integrated Devices, Center for Integrated Circuits, University of Electronic Science and Technology of China, Chengdu 611731, China
[2]Department of Signal Theory and Communications, University of Alcalá, 28871 Alcalá de Henares, Spain

Corresponding authors: Huizhen Jenny Qian (huizhenqian@hotmail.com) and Xun Luo (xun-luo@ieee.org)

This work was supported in part by the National Natural Science Foundation of China under Grant 61934001 and Grant 61904025.

ABSTRACT In this paper, two types (i.e., type-A and type-B) of hybrid microstrip/defected ground structure (DGS) cells are proposed for passive circuit implementation with ultra-wide stopband. Both cells consist of the stepped-impedance DGS and embedded folded slotline on the ground, which could obtain the dual-resonances. In type-A cell, a microstrip T-stub on the top side is introduced, which can not only allocate a strong coupling to the DGS with slotline on the bottom side, but also act as the input/output port. To finely adjust the dual-resonances of the type-B cell, a grounded microstrip patch is used. Meanwhile, such compact cells could feature an ultra-wide upper stopband, due to their own slow-wave effect. Based on the aforementioned hybrid microstrip/DGS cells, two dual-band bandpass filters (BPFs) and a dual-band filtering power divider (FPD) are proposed and fabricated. Measured and simulated results are in a fairly-close agreement. Both dual-band BPFs exhibit the ultra-wide upper stopband, which extends up to 40 GHz with a high rejection level about 30 dB. Besides, the dual-band FPD has merits of more than 18.7 dB of in-band isolation and 28 dB stopband rejection levels up to 40 GHz.

INDEX TERMS Bandpass filter (BPF), defected ground structure (DGS), dual-band filter, filtering power divider (FPD), slow-wave, ultra-wide stopband.

I. INTRODUCTION

With the ever-increasing demands of modern high-speed and multi-function wireless communication systems, the trend to support various communication standards and operate at multiple frequency bands in one system is continuously developed [1], [2]. The multi-mode resonators have been carried out and applied in wideband RF/microwave systems [3]. However, the inter-system interference caused by harmonics is becoming a common and important issue, which should be suppressed. Recently, the circuit design utilized basic physical properties has taken over using electromagnetic compatibility (EMC) rules blindly [4]. Meanwhile, suppressing the spurious passbands is an effective method to improve the multifunctional system performances [5]. Nevertheless, the design of passive components with ultra-wide upper stopband for multi-function systems should be further developed.

As a critical component in microwave communication systems, the bandpass filter (BPF) with wide stopband is widely developed. In order to obtain the good out-of-band attenuation, the floating ground-plane [6], wiggly line [7], parallel coupled-line [8], and defected ground structure (DGS) [9] are proposed to suppress the first spurious passband. To extend the stopband bandwidth, the multi-order coupled-line [10], periodic DGSs [11], and stepped-impedance resonators (SIRs) [12] have been introduced. Nevertheless, the spurious passbands are suppressed less than $10f_0$ (where f_0 stands for the center frequency of passband), due to the restriction of the fabrication. To further enhance the stopband performance, a novel and simple slow-wave resonant cell is presented [13], which has instinct fundamental resonance with an ultra-wide stopband response. Based on such resonant cell, filters with more than $10f_0$ spurious suppression could be easily achieved.

The associate editor coordinating the review of this manuscript and approving it for publication was Nagendra Prasad Pathak.

However, such filter can only introduce a single passband. To satisfy the various wireless standards, the multi-layer organic substrate [14], SIRs [15], [16], and net-type resonators [17] are proposed to achieve dual-band with a wide stopband. However, the stopband bandwidth is relatively narrow, where the in-band performance still requires further improvement. Therefore, the design of dual-band BPF with the merits of sharp-rejection capabilities, low in-band insertion loss, ultra-wide upper stopband, and miniaturized size still remains great challenges.

Meanwhile, the power dividers [18]–[24] and BPFs usually coexist in the same RF front-end, thus, the filtering power divider (FPD) already draws great attentions. In order to achieve a good out-of-band performance, the looped coupled-line is developed [18]. Then, to extend the stopband bandwidth, two lowpass filters attached in the output sections [19] and hybrid microstrip/DGS cell with spurious suppression [20] are introduced. However, these FPDs could not meet the requirements of modern multi-band standards. In [21]–[23], the coupled SIRs and dual-resonance resonators are used to achieve dual-band response, whereas the stopband bandwidth still needs to be extended. Therefore, the dual-band FPDs with the ultra-wide stopband and good rejection level should be dramatically developed.

In this paper, two novel dual-resonance hybrid microstrip/DGS cells (i.e., type-A and type-B) are proposed and investigated, following our previous work [25]. Such cells can not only allocate adjustable dual-resonances, but also achieve a strong slow-wave effect for a wideband harmonic suppression. Meanwhile, a whole analytical framework about the dual-resonances hybrid microstrip/DGS cells is firstly given, while the physical meaning of the DGS is proposed for better logical readability. Then, the EM fields of folded shape DGS are investigated, which could exhibit the instinct characteristic of the radiation suppression. Therefore, the radiation loss could be reduced by such hybrid microstrip/DGS cells when compared to conventional DGS. Moreover, this implementation can minimize the circuit size of the proposed cell. For practical applications, a series of passive circuits (i.e., the dual-band BPFs and FPD) is developed based on the proposed hybrid microstrip/DGS cells. The measured results demonstrate the feasibility of such cells in realizing the dual-band passive circuits with merits of good passband insertion loss, high passband selectivity, and ultra-wide stopband with strong spurious suppression. The organization of the rest of the paper is as follows: in Section II, a detailed description of the proposed two types dual-resonance hybrid microstrip/DGS cells is proposed. Section III illustrates the operation of coupled cells with various schemes. Then, Section IV presents the application examples of two types dual-band BPFs and a dual-band FPD with ultra-wide stopband. Finally, a brief conclusion is given in Section V.

II. HYBRID MICROSTRIP/DGS DUAL-RESONANCE CELL

Fig. 1 depicts the configurations of the proposed dual-resonance hybrid microstrip/DGS cells. On the bottom side of the substrate, the stepped-impedance DGS with embedded folded slotline is proposed. Then, two types of microstrip structures are introduced for implementing the hybrid microstrip/DGS cells (i.e., type-A and type-B). As shown in Fig. 1(a), a microstrip T-stub is introduced on the top side in type-A cell. As for the type-B cell, a grounded microstrip patch is proposed, which is shown in Fig. 1(b). To investigate the electrical characteristics of the proposed cells, the full-wave EM simulator IE3D and RT5880 dielectric substrate (i.e., the dielectric constant $\epsilon_r = 2.2$ with a thickness of $h = 0.508$ mm) are used.

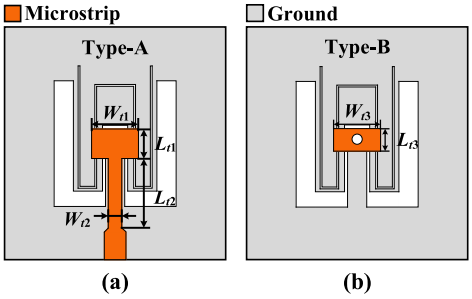

FIGURE 1. Configurations of both types dual-resonance hybrid microstrip/DGS cells. (a) Type-A cell. (b) Type-B cell.

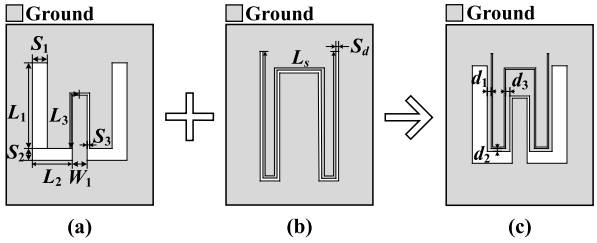

FIGURE 2. Configurations of (a) the stepped-impedance DGS, (b) the folded slotline, and (c) the dual-resonance DGS cell ($L_1 = 7.45$, $L_2 = 3.5$, $L_3 = 3.85$, $L_s = 34.5$, $S_1 = 1.3$, $S_2 = 1.05$, $S_3 = 0.1$, $S_d = 0.1$, $d_1 = 0.25$, $d_2 = 0.25$, and $d_3 = 0.2$, unit: mm).

A. DUAL-RESONANCE

1) DUAL-RESONANCE CHARACTERISTICS

Such two proposed types cells (i.e, type-A and type-B) could both generate dual-resonances. Note that, these two fundamental frequencies for the proposed cells are mainly determined by the DGS cell on the bottom side. Here, the dual-resonances (i.e., f_{sdgs} and f_{slot}) are allocated by the stepped-impedance DGS in Fig. 2(a) and folded slotline in Fig. 2(b), respectively. Based on the derivation processes in the Appendix A, these two resonant frequencies at f_1 and f_2 of the proposed DGS in Fig. 2(c) can be defined as

$$f_1 = \sqrt{\frac{M_1 + \sqrt{M_1^2 - 4M_2}}{2}} \tag{1}$$

$$f_2 = \sqrt{\frac{M_1 - \sqrt{M_1^2 - 4M_2}}{2}} \tag{2}$$

where

$$M_1 = f_{sdgs}^2 + f_{slot}^2 + \frac{m_d^2 f_{sdgs} f_{slot}}{\gamma_{sdgs}\gamma_{slot}} \tag{3}$$

$$M_2 = f_{sdgs}^2 f_{slot}^2. \tag{4}$$

The γ_{sdgs} and γ_{slot} are the parameters that define the transformations of the stepped-impedance DGS and folded slotline, respectively. Meanwhile, the m_d is the coupling coefficients for these two resonators. To determine these parameters, the same technique is used as in [26]–[27].

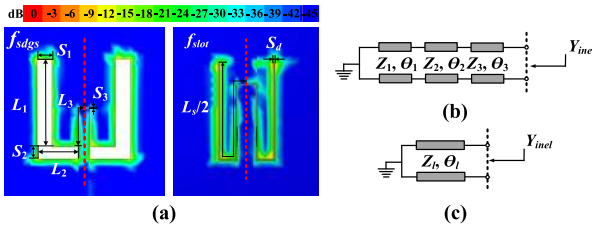

FIGURE 3. (a) EM-simulated electric current density distributions of slotline and stepped-impedance DGS. The simplified even-mode equivalent circuits of (b) the stepped-impedance DGS and (c) the slotline.

It is known that the etched defect in a DGS disturbs the shield current distribution on the ground [28], and thus the stepped-impedance DGS and folded slotline possess their own resonant frequencies on the ground. To discuss the f_{sdgs} and f_{slot}, Fig. 3(a) shows the EM-simulated electric current density of the stepped-impedance DGS and folded slotline. It is notable that the current is concentrated on its edges at the fundamental resonance (i.e. f_{sdgs} and f_{slot}). The current density is distributed symmetrically along the dotted line. Then, the simplified equivalent circuits can be derived. Note that, the dual-resonances of the proposed resonant cells are determined by the even-mode resonances of the stepped-impedance DGS and folded slotline. Therefore, the even-mode equivalent circuits are introduced to discuss the dual-resonances operation, as shown in Fig. 3(b) and (c), respectively. Then, the even-mode input admittances (i.e., Y_{ine} and Y_{inel}) are derived in the equation (5), as shown at the bottom of this page, and (6) as

$$Y_{inel} = \frac{1}{jZ_l \tan\theta_l}. \tag{6}$$

The resonance conditions for these two resonators are $Y_{ine} = 0$ and $Y_{inel} = 0$, respectively. Meanwhile, the electrical length and characteristic impedance of the stepped-impedance DGS could be extracted from the pole-splitting method [29] in conjunction with full-wave simulations. The Z_l and θ_l are defined by the equations in Appendix B. Therefore, the relationships between the physical dimension of DGS cell and its resonant frequencies could be obtained

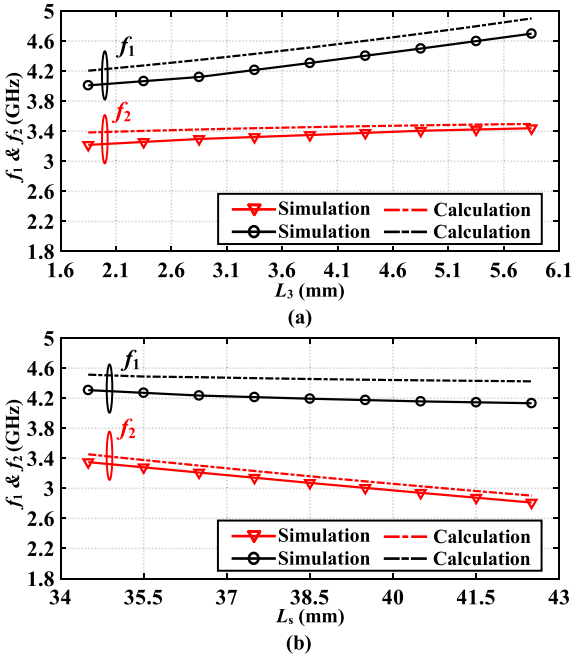

FIGURE 4. (a) Resonances of the DGS cell versus the L_3 (L_s = 34.5 mm). (b) Resonances of the DGS cell versus the L_s (L_3 = 3.85 mm).

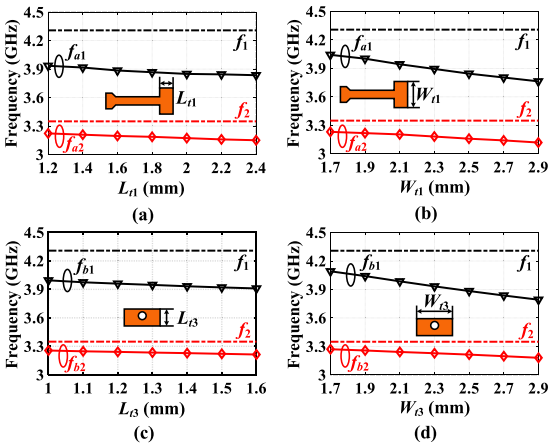

FIGURE 5. (a) Effects of the dimension L_{t1} on the fundamental resonant frequencies f_{a1} and f_{a2} (W_{t1} = 2.5 mm). (b) Effects of the dimension W_{t1} on the fundamental resonant frequencies (L_{t1} = 2.2 mm). (c) Effects of the dimension L_{t3} on the fundamental resonant frequencies f_{b1} and f_{b2} (W_{t3} = 2.3 mm). (d) Effects of the dimension W_{t3} on the fundamental resonant frequencies (L_{t3} = 1.4 mm).

based on the equations (1)–(6). Then, the dual-resonances for the proposed DGS cell versus the different dimensions (i.e., L_3 and L_s) are depicted in Fig. 4(a) and (b), respectively. It can be seen that the calculated and EM-simulated results are in close-agreement with a similar variation profile.

$$Y_{ine} = \frac{1}{jZ_3} \cdot \frac{Z_3(Z_2 - Z_1\tan\theta_1\tan\theta_2) - Z_2\tan\theta_3(Z_1\tan\theta_1 + Z_2\tan\theta_2)}{Z_2(Z_1\tan\theta_1 + Z_2\tan\theta_2) + Z_3\tan\theta_3(Z_2 - Z_1\tan\theta_1\tan\theta_2)} \tag{5}$$

2) LOADING EFFECT

The fundamental resonances (i.e., f_1 and f_2) are shifted down due to the loading effect of microstrip T-stub and grounded patch in type-A and type-B cells, respectively. Then, to verify the effects on resonant frequencies, the variation tendencies of these two fundamental resonances associated to the type-A cell are depicted in Fig. 5(a) and (b), which show the curves of f_{a1} and f_{a2} against the dimensions W_{t1} and L_{t1}, respectively. Meanwhile, the curves of the EM-simulated f_{b1} and f_{b2} versus different geometrical parameters W_{t3} and L_{t3} for type-B cell are shown in Fig. 5(c) and (d), respectively. It can be seen that the fundamental resonant frequencies f_{a1} and f_{a2} decrease while the L_{t1} or W_{t1} are increased. Therefore, the required resonances can be obtained by finely tuning the dimensions of microstrip T-stub. The feed-line tapped on the microstrip T-stub could be utilized as 50-Ω input/output port for this cell. Besides, the f_{b1} and f_{b2} are decreased, once the grounded patch is enlarged. Thus, the specific frequencies of type-B cell could be obtained by finely adjusting the microstrip patch.

B. SPURIOUS SUPPRESSION

1) SLOW-WAVE EFFECT

As a further merit of the proposed dual-resonance DGS, a wide stopband operation could be achieved. It is well known that the characteristic impedance of the slotline/DGS is mainly determined by the width. As the slot width is enlarged, its effective inductance increases and effective capacitance decreases. Then, the required distributions of effective inductance and capacitance are obtained by finely adjusting the geometric dimensions, especially the inductance. Therefore, the proposed DGS resonant cells can be designed as an approximate *LC*-resonator with a wide stopband operation as shown in [30]. The simulated transmission response and the EM-simulated current destiny distributions at stopband are depicted in Fig. 6. In this case, two regions (i.e., Reg. I and Reg. II) in DGS are concerned at the stopband frequencies f_{ds1}, f_{ds2}, f_{ds3}, and f_{ds4}. It is found that the electric-field (i.e., *E*-field) is highly concentrated on the thin slot in Reg. I, which achieves strong effective capacitance. Then, the *E*-field nearly disappears in Reg. II, which means that the large effective inductance is developed. By the transmission line theory, the propagation constant of a line without loss is

$$\beta = \omega_0 \sqrt{LC} \tag{7}$$

where ω_0 is the angular frequency, L and C are the distributed shunt capacitance and series inductance per unit length, respectively. It shows that slow-wave effect (large propagation constant) can be achieved by increasing L and C [31]. As for the proposed dual-resonance DGS resonator, the series connection of such high effective capacitance and inductance could achieve a strong slow-wave effect. As proved in [32], the resonator with slow-wave effect can be used to design the bandpass filter with a wide upper stopband.

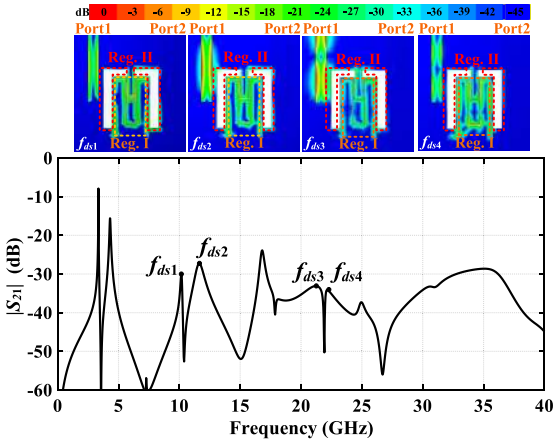

FIGURE 6. Simulated power transmission response ($|S_{21}|$) of the proposed dual-resonance DGS cells and the EM-simulated electric current density distributions.

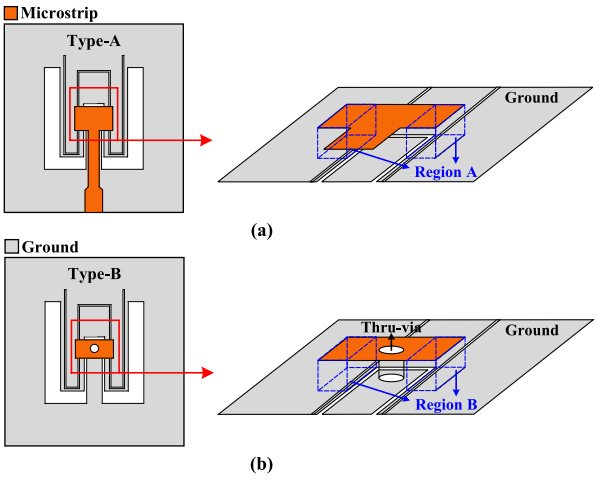

FIGURE 7. Configurations of the proposed structure. (a) Type-A cell. (b) Type-B cell.

2) SLOW-WAVE EFFECT ENHANCEMENT

Due to the constraints on planar structures, the large effective capacitance is achieved by an ultra-narrow slot, while the implementation is limited by the printed circuit board (PCB) fabrication. To further improve the stopband performance, the slow-wave could be enhanced by the proposed hybrid microstrip/DGS. As shown in Fig. 7, a microstrip T-stub and grounded microstrip patch are located above the dual-resonance DGS in type-A and type-B cells, respectively. In this case, such two microstrip structures could introduce a strong vertical capacitive effect in Region A and B. Thus, as the further merits of the hybrid microstrip/DGS, the specific distributions of the effective capacitance can be used for a relatively stronger slow-wave effect. Then, the propagation constant is increased, which leads to an enhanced stopband performance.

To verify the ultra-wide upper-stopband operation, the power transmission responses with related electrical current densities are shown in Fig. 8. Note that, the spurious is

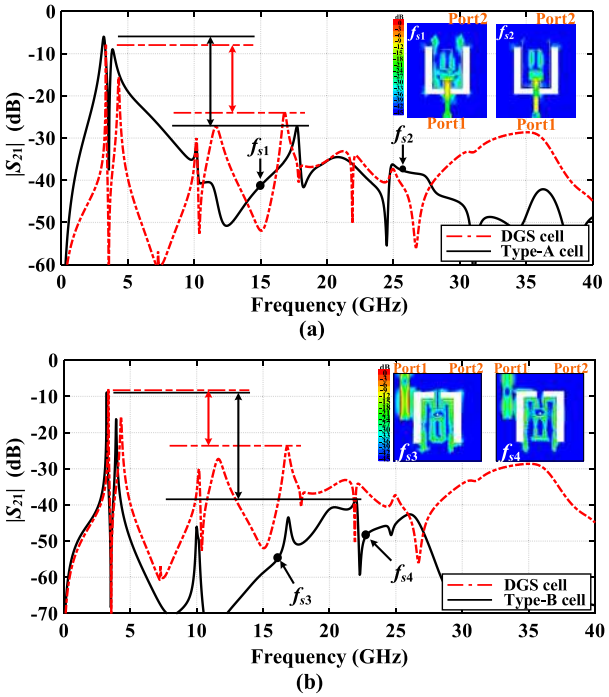

FIGURE 8. Simulated power transmission response ($|S_{21}|$) of the proposed slow-wave cells and EM-simulated electric current density distributions at f_{s1}, f_{s2}, f_{s3}, and f_{s4}. (a) Type-A dual-resonance cell. (b) Type-B dual-resonance cell.

suppressed with higher rejection level in both dual-resonance hybrid microstrip/DGS cells (i.e., type-A and type-B), due to the enhanced slow-wave effect. In Fig. 8(a), the E-field is highly concentrated on the microstrip T-stub, which indicates that a stronger effective capacitance can be achieved in type-A cell at two stopband frequencies f_{s1} and f_{s2}. Thus, a larger propagation constant (i.e., β) can be introduced by the series connection of such high effective capacitance and inductance. Then, an ultra-wide upper-stopband with a high rejection level is introduced by such cell (i.e., type-A). In addition, Fig. 8(b) depicts the transmission response of type-B cell, including the EM-simulated electric current densities at two stopband frequencies f_{s3} and f_{s4}. The E-field is highly concentrated on grounded microstrip patch, which introduces a strong effective capacitance. Therefore, similar as the type-A cell, an ultra-wide upper stopband with high rejection level could be achieved by the type-B cell.

C. RADIATION LOSS

Owing to the interference effect of the induced magnetic-field (i.e., H-field) in the parallel slotline/DGS portions, the radiation loss could be minimized. Fig. 9(a) sketches the E-filed and H-field distributions in cross-section. It is found that the E- and H-fields exist around the cross-section of the gaps. Note that, the E-field potential difference between the two conductors of the gap is shown in Fig. 9(b). Meanwhile, the direction of H-field is kept identical along the longitudinal direction of the gap [33]. Based on these principles, the E- and H-fields of these two resonant parts (i.e., folded DGS

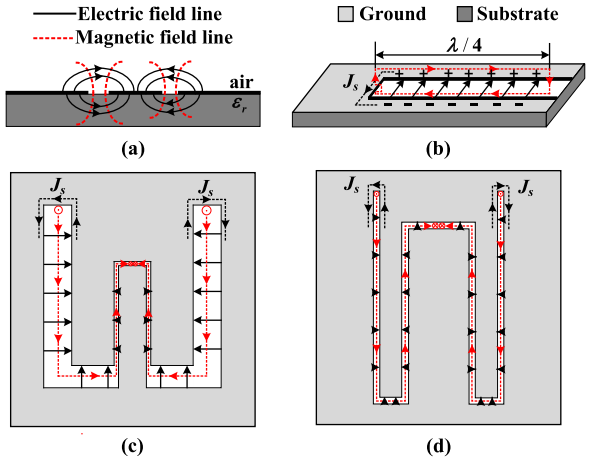

FIGURE 9. (a) Field distributions on the parallelized slotline in cross-section. (b) Field and current distributions in vicinity of a slotline short end. (c) Field distributions of the stepped-impedance DGS. (d) Field distributions of the folded slotline.

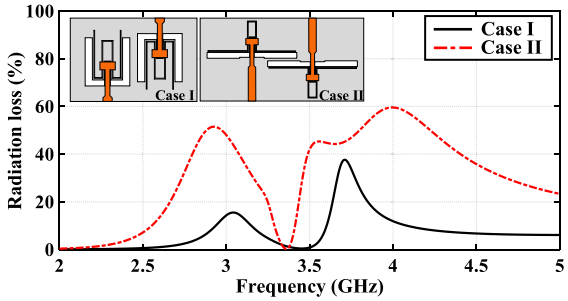

FIGURE 10. Calculated radiation loss of folded and unfolded structures.

and slotline) at their own resonant frequencies are depicted in Fig. 9(c) and (d), respectively. It can be seen that the H- and E-field lines around the folded part are almost in opposite directions in the two parallel portions. As proved in [34], the radiations can be reduced, due to the interference of these two oppositely-oriented H-field intensities. Besides, the equivalent electrical length of the DGS/slotline could be decreased owing to this effect. Nevertheless, the current flows in the metal surface around the end of the gap, and there is appreciable energy stored beyond the termination. The related appearances are depicted in Fig. 9(b), (c), and (d), respectively. Thus, the net result is that the equivalent electrical length of the slotline/DGS will be increased [35]. To verify the low radiation characteristic of the proposed structures, two cases are discussed here with different shapes. Case I is two coupled type-A cells, while Case II represents the unfolded case, as shown in Fig. 10. Meanwhile, the radiation loss can be calculated by the following equation

$$R_r = 1 - |S_{11}|^2 - |S_{21}|^2. \tag{8}$$

As proved in Fig. 10, it can be seen that proposed folded structure could effectively reduce the radiation loss. Meanwhile, such implementation could minimize the circuit size for proposed cell.

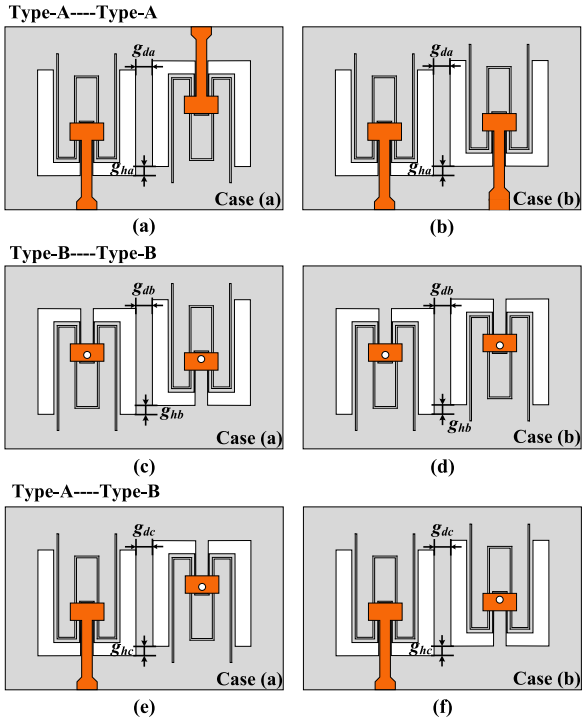

FIGURE 11. Configurations of these two types resonant cells coupled in Case (a) and Case (b). Case (a): interdigital coupled scheme, Case (b): combline coupled scheme.

III. HYBRID MICROSTRIP/DGS CELLS WITH QUASI-COUPLED SCHEMES

Based on the proposed dual-resonance cells (i.e., type-A and type-B), the coupled schemes are introduced and investigated. Note that, a strong coupling between these two cells could be generated when they are close to each other. To verify the relationship between coupling coefficient and physical dimension, two cases are discussed in this paper. Case (a) represents two proposed cells with an interdigital-coupled scheme, while Case (b) is the combine-coupled scheme. The configurations for these two coupled resonant cells with different coupled schemes are shown in Fig. 11, respectively. Meanwhile, the coupling coefficients (i.e., k_{ij}) for the synchronous and asynchronous cases [29] can be derived as follow:

$$k_{ij} = \frac{f_{pi}^2 - f_{pj}^2}{f_{pi}^2 + f_{pj}^2} \tag{9}$$

$$k_{ij} = \frac{1}{2}\left(\frac{f_{0i}}{f_{0j}} + \frac{f_{0j}}{f_{0i}}\right)\sqrt{\left(\frac{f_{pi}^2 - f_{pj}^2}{f_{pi}^2 + f_{pj}^2}\right)^2 - \left(\frac{f_{0i}^2 - f_{0j}^2}{f_{0i}^2 + f_{0j}^2}\right)^2} \tag{10}$$

where f_{0i} and f_{0j} are the resonant frequencies in the absence of coupling, and the f_{pi} and f_{pj} are these two dominant resonant frequencies under the coupled conditions.

To verify the coupling strength for these two coupled schemes, the extracted coupling coefficients associated to these coupled schemes versus the gaps (i.e., $g_{da,b,c}$ and $g_{ha,b,c}$) are compared in Fig. 12. It is notable that the coupling

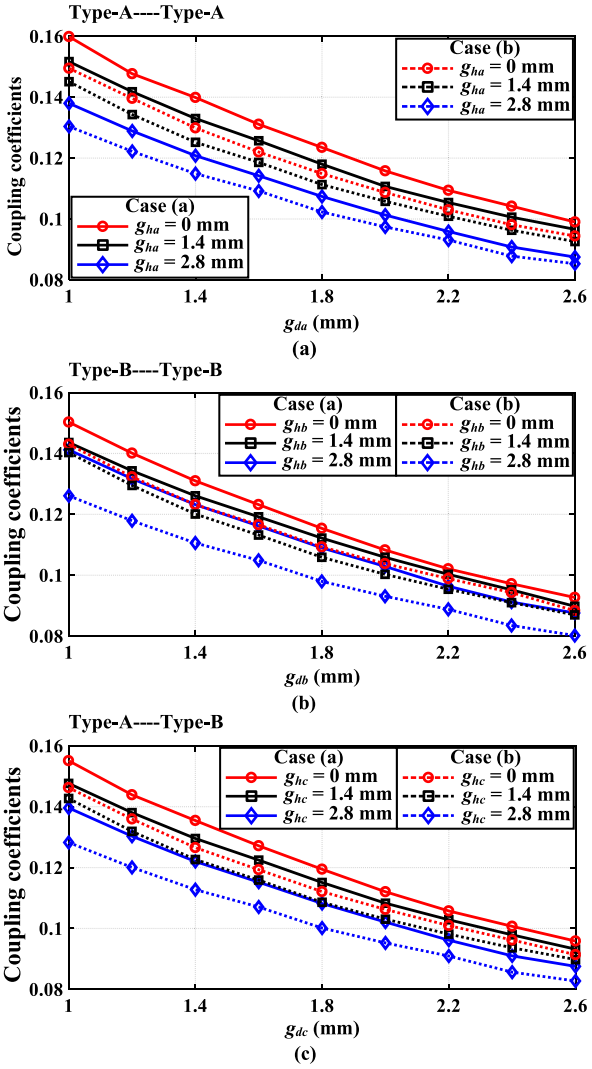

FIGURE 12. Coupling coefficients versus the distances between two coupled cells. (a) Coupled type-A cells. (b) Coupled type-B cells. (c) Coupled type-A and type-B cells.

coefficients between those two coupled cells are mainly depended on the gaps. As the gaps increase, the coupling coefficients decrease. Therefore, once the gaps between two cells are carefully selected, the desired coupling coefficients could be obtained. Meanwhile, it is found that the interdigital-coupled scheme can introduce a stronger coupling than the combline-coupled scheme under the same coupled schemes. Thus, the interdigital-coupled scheme could be utilized in a relatively stronger coupling condition, while the combline-coupled scheme is used for the case of weaker coupling.

IV. DESIGN EXAMPLES

To verify the practical implementation of such dual-resonance hybrid microstrip/DGS cells (i.e., type-A and type-B) in the realization of dual-band passive components, the dual-band BPFs and dual-band FPD with ultra-wide upper stopband are proposed and fabricated. The RT5880 dielectric

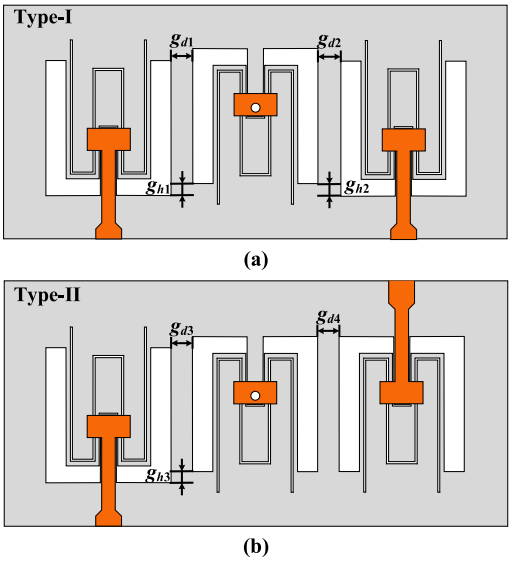

FIGURE 13. Configurations of the proposed three-order dual-band BPFs ($g_{d1} = g_{d2} = g_{d3} = 1.5$, $g_{d4} = 1.3$, and $g_{h1} = g_{h2} = g_{h3} = 1.25$, unit: mm). (a) Type-I dual-band BPF. (b) Type-II dual-band BPF.

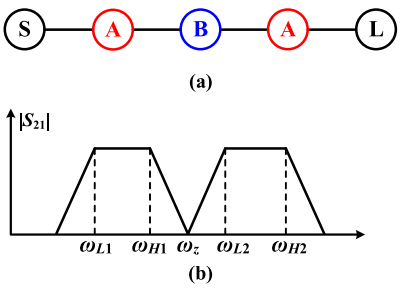

FIGURE 14. (a) Coupling-routing diagram of the proposed three-order dual-band BPFs. (b) Conceptual transmission response ($|S_{21}|$) for the dual-band BPFs.

substrate (i.e., $\epsilon_r = 2.2$ with a thickness of $h = 0.508$ mm) and the Agilent N5244A PNA-X Network Analyzer are utilized for the circuit manufacturing and measurement, respectively. By featuring the sharp-rejection dual-passband and ultra-wide upper stopband characteristics, the proposed dual-band BPFs and FPD are attractive for practical applications in dual-band RF systems with closely-spaced operational bands.

A. DUAL-BAND BPF DESIGN

Based on the dual-resonance hybrid microstrip/DGS cells, two prototypes of three-order dual-band BPFs are proposed, as shown in Fig. 13. It can be seen that each filter consists of three resonant cells. The first and third resonance cells are the type-A scheme, whereas the second one is a type-B cell. As depicted in Fig. 13(a), the cells of the first dual-band BPF is implemented with an interdigital-coupled schemes. Meanwhile, the interdigital- and combline-coupled schemes are introduced to form the second dual-band BPF based on the three cells, as shown in Fig. 13(b). Here, the coupling-routing diagram related to these two BPFs are exhibited in Fig. 14(a).

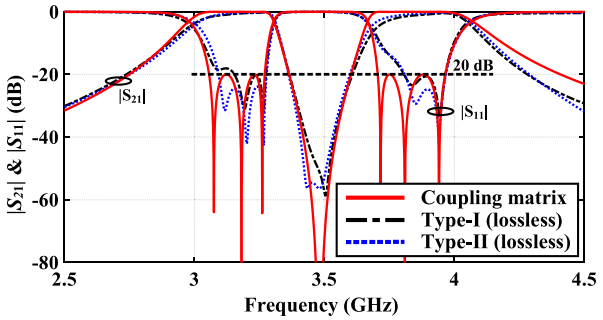

FIGURE 15. Lossless simulated and synthesized power transmission ($|S_{21}|$) and reflection ($|S_{11}|$) responses of the dual-band BPFs (in-band details).

Note that, the dual-resonance of the type-A and type-B cells are optimized to be same for the filter design. According to the equations in Appendix A, the transformed frequencies are expressed as follow:

$$\Omega_{dual_A(\omega)} \approx \Omega_{dual_B(\omega)} = \frac{\gamma_a\gamma_b(\omega^2-\omega_a^2)(\omega^2-\omega_b^2) - k_{cell}^2\omega_a\omega_b\omega^2}{\gamma_b\omega_a\omega(\omega^2-\omega_b^2)} \quad (11)$$

where k_{cell} is the coupling coefficient between two resonators, the γ_a and γ_b are the parameters that define the transformations of these two resonators, and the parameters ω_a and ω_b are resonant frequencies of these two resonators (i.e., stepped-impedance DGS and folded slotline) in the absence of coupling, respectively. Then, the frequency response for the dual-band BPFs can be determined by five frequency parameters [26] and [36]: ω_{L1}, ω_{L2}, ω_z, ω_{H1}, and ω_{H2}, as shown in Fig. 14(b). Here, the ω_{L1} and ω_{H1} define the lower passband, while the ω_{L2} and ω_{H2} determine the upper one. These passbands are separated by means of an inter-band transmission zero at ω_z. Then, the frequencies ω_a and ω_b, parameters γ_a and γ_b, and k_{cell} can be derived by formulas in Appendix C. Since the proposed dual-band BPFs are developed with a Chebyshev response. The g_i (i.e., $i = 1, 2, 3, \cdots$) is the low-pass prototype parameter. Thus, the coupling coefficients between the proposed cells can be obtained as

$$k_{AB} = \frac{1}{\gamma_a\sqrt{g_i g_{i+1}}} \qquad i = 1, 2. \quad (12)$$

To verify the aforementioned synthesis mechanism, two types of dual-band BPFs with the frequency parameters of $f_{L1} = 3.06$ GHz, $f_{H1} = 3.27$ GHz, $f_{L2} = 3.70$ GHz, $f_{H2} = 3.96$ GHz, and return loss of 20 dB in each band are proposed. The center frequencies of the resonators, γ_a, and γ_b are derived as: $f_a = 3.4835$ GHz, $f_b = 3.4759$ GHz, $\gamma_a = 7.4117$, and $\gamma_b = 4.2219$. Then, the coupling coefficients are calculated as: $k_{AB} = 0.1391$ and $k_{cell} = 0.1788$. Thus, the passband coupling matrix $[A]$ can be expressed by [37]

as follow:

$$[A] = \begin{bmatrix} -j & 0.7820 & 0 & 0 & 0 \\ 0.7820 & \Omega_{dual_A} & 0.5379 & 0 & 0 \\ 0 & 0.5379 & \Omega_{dual_B} & 0.5379 & 0 \\ 0 & 0 & 0.5379 & \Omega_{dual_A} & 0.7820 \\ 0 & 0 & 0 & 0.7820 & -j \end{bmatrix}. \tag{13}$$

Meanwhile, the theoretical S-parameters (i.e., red-curves) associated to the coupling matrix are shown in Fig. 15. While compared to such lossless results, both the calculation and EM-simulation show a fairly-close agreement.

The design procedures of the proposed dual-band BPFs can be summarized as follow. The first step is to obtain the initial sizes of two types cells. Equations in Appendix C can be used to derive the specific resonant frequencies and coupling coefficients for the stepped-impedance DGS and folded slotline, respectively. Besides, Fig. 16(a) and (b) depict the extracted internal coupling coefficients of the type-A and type-B cells versus the d_{1-A} and d_{1-B}, respectively. Then, the physical gaps (i.e., d_{1-A} and d_{1-B}) between the stepped-impedance DGS and folded slotline are used to adjust the coupling coefficients (i.e., k_{cell-A} and k_{cell-B}). In addition, the required resonances of stepped-impedance DGS and folded slotline are obtained by the equations (5) and (6). Thus, the geometries related to both cells can be determined by finely adjust its dimensions. The second step is to achieve the internal couplings coefficients between the dual-resonance cells. In this case, the gaps (i.e., $g_{da,b,c}$ and $g_{ha,b,c}$ in Fig. 11) can be properly adjusted to achieve specific coupling coefficient for the passband response. The third step is to meet the required quality factors for both passbands. The design curves of Q_{el} and Q_{eh} against W_{t1} can be obtained by the methods in [29], which are depicted in Fig. 16(c) and (d), respectively. With properly optimized dimensions of the microstrip T-stub, the required external quality factors for the dual-band operation can be achieved.

According to the design procedure mentioned above, two dual-band BPFs (i.e., BPF-I and BPF-II) are fabricated, as shown in Fig. 17. The simulated and measured S-parameters of the proposed filters are depicted in Fig. 18. As can be seen, the BPF-I operates at $f_1 = 3.17$ GHz and $f_2 = 3.91$ GHz with the 3-dB fractional bandwidth (FBW) of 8.4% and 7.1%, respectively. Note that, the operational bands corresponded to BPF-II have slightly shifted. The measured center frequencies of the passbands in BPF-II are 3.16 and 3.90 GHz with the 3-dB FBW of 8.5% and 7.1%, respectively. The minimum in-band insertion loss levels for the lower and upper passbands are less than 1.76 and 1.63 dB in BPF-I, 1.87 and 1.67 dB in BPF-II. With the strong slow-wave effect, both filters can feature an ultra-wide upper stopband up to 40 GHz with a high rejection level greater than 28 dB and 30 dB for both BPFs, respectively. In addition, the fabricated prototype related to BPF-I has a compact core circuit size of 27 mm $\times$ 12.25 mm (i.e., $0.389\lambda_g \times 0.177\lambda_g$, where λ_g is the microstrip guided wavelength at the center frequency of the first passband). The core circuit size of BPF-II is 26.9 mm $\times$ 14.75 mm (i.e., $0.385\lambda_g \times 0.213\lambda_g$, where λ_g is the microstrip guided wavelength at the center frequency of the first passband). Table 1 compares the proposed dual-band BPFs with the state-of-the-arts dual-band BPFs [14]–[17], which are with a wide upper stopband. It is notable that the proposed dual-band BPFs with closely-spaced passbands have merits of the broader upper stopband bandwidth and lower in-band insertion loss.

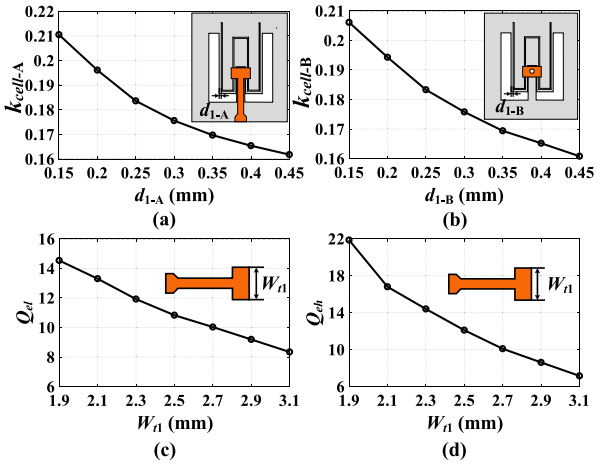

FIGURE 16. (a) Effects of the dimension d_{1-A} on the k_{cell-A}. (b) Effects of the dimension d_{1-B} on the k_{cell-B}. (c) Effects of the W_{t1} on Q_{el} (L_{t1} = 2.2 mm). (d) Effects of the W_{t1} on Q_{eh} (L_{t1} = 2.2 mm).

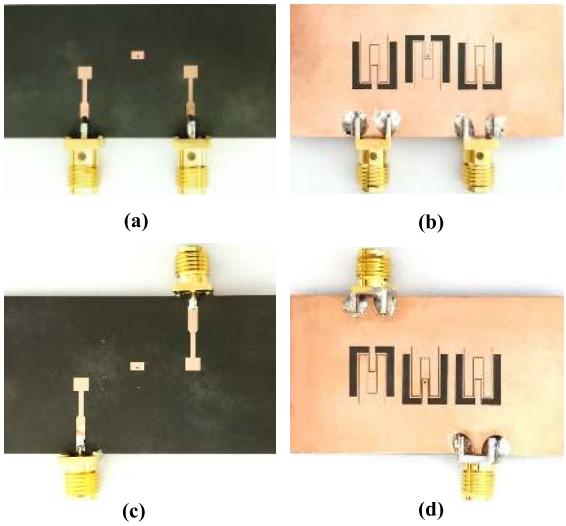

FIGURE 17. Photographs of the developed dual-band BPF prototypes. (a) Top view and (b) bottom view of Type-I BPF. (c) Top view and (d) bottom view of Type-II BPF.

B. DUAL-BAND FPD DESIGN

As the second design example of the conceived dual-resonance cells, an original dual-band FPD is proposed, as depicted in Fig. 19. For the design of power divider part, two $\lambda/4$ microstrip lines are tapped on the arms of the traditional Wilkinson power divider. Meanwhile, two resistors

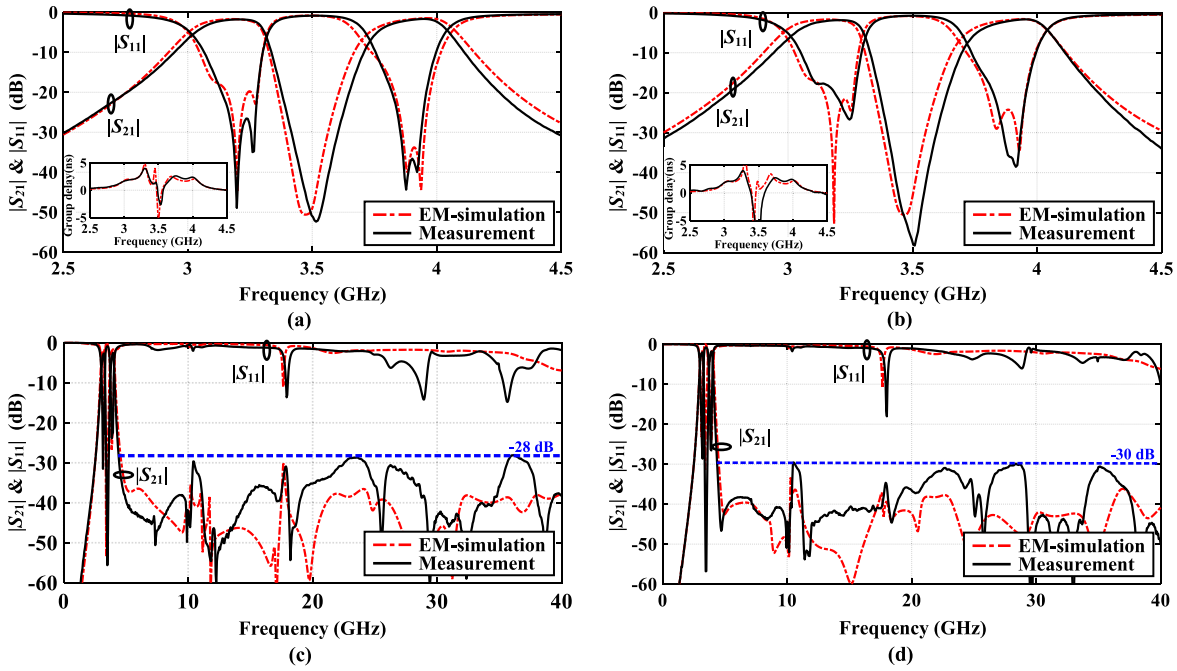

FIGURE 18. Measured and simulated transmission ($|S_{21}|$), reflection ($|S_{11}|$), and grounp delay of the developed dual-band BPF prototypes ($d_1 = 0.25$, $d_2 = 0.25$, $d_3 = 0.2$, $g_{d1} = g_{d2} = g_{d3} = 1.5$, $g_{d4} = 1.3$, $g_{h1} = g_{h2} = g_{h3} = 1.25$, $L_1 = 7.45$, $L_2 = 3.5$, $L_3 = 8.45$, $L_s = 34.5$, $L_{t1} = 2.2$, $L_{t2} = 4.05$, $L_{t3} = 1.4$, $S_1 = 1.3$, $S_2 = 1.05$, $S_3 = 0.1$, $S_d = 0.1$, $W_1 = 1$, $W_{t1} = 2.5$, $W_{t2} = 0.8$, and $W_{t3} = 2.3$, unit: mm). (a) In-band details of BPF-I. (b) In-band details of BPF-II. (c) Wideband response of BPF-I. (d) Wideband response of BPF-II.

TABLE 1. Comparison of the dual-band BPF with the state-of-the-art.

Reference	[14]	[15]	[16]	[17]	Type-I	Type-II
f_1/f_2* (GHz)	1.7/4	2.4/5.2	2.4/6	1/2	**3.17/3.91**	**3.16/3.90**
Passband Ratio (f_2/f_1)	2.35	2.17	2.5	2	**1.23**	**1.23**
3-dB FBW (%)	20/18	10.6/6	5/4.7	4.6/4.8	**8.4/7.1**	**8.5/7.2**
Insertion Loss (dB)	6.7/6.5	2.27/2.88	1.85/2.98	2.65/2.44	**1.76/1.63**	**1.87/1.67**
Return Loss (dB)	>11/12	>8.9/9	N/A	>12.6/12.6	**>20/20**	**>18/20**
Lower Passband Roll-Off (dB/GHz)	320/311**	67/77**	132/165**	433/355**	**48/240**	**49/267**
Upper Passband Roll-Off (dB/GHz)	223/185**	72/76**	143/134**	332/283**	**171/58**	**166/68**
Stopband Bandwidth	Up to 16.5 GHz	Up to 9 GHz	Up to 20 GHz	Up to 5.6 GHz	**Up to 40 GHz**	**Up to 40 GHz**
Stopband Rejection Level (dB)	>50	>32.2	>30	>20	**>28**	**>30**
Size ($\lambda_g \times \lambda_g$)	0.4×0.05	N/A	N/A	N/A	**0.389×0.177**	**0.385×0.213**

*f_1 and f_2 stand for the center frequencies of lower and upper passbands, respectively.
**Calculated from the measured results.

(i.e., R_1 and R_2) are embedded in such two microstrip lines, which can generate two transmission zeros for the enhanced isolation from Port2 to Port3 [38]. Then, to achieve a dual-band filtering response with an ultra-wide upper stopband, the proposed BPFs are directly connected at the end of the power divider part. Therefore, such scheme can not only achieve a dual-band FPD, but also obtain the wideband output isolation and harmonic suppression at the stopband. To discuss the characteristics corresponded to the proposed power divider part, the simplified equivalent circuits are introduced. The even-mode equivalent circuit of the power divider part is shown in Fig. 20(a). In this case, the output-isolation resistors are viewed as open circuits. Then, the odd-mode equivalent circuit is depicted in Fig. 20(b), where the resistors are equivalently grounded. Thus, the theoretical S-parameters for this three-port network can be derived as follow:

$$S_{11} = S_{11}^e = \left|\frac{Z_{in1e} - 2Z_{p1}}{Z_{in1e} + 2Z_{p1}}\right| \tag{14}$$

$$S_{21} = S_{31} = \frac{S_{12}^e}{\sqrt{2}} = \frac{\sqrt{2}}{2}\sqrt{1 - \left|\frac{Z_{in1e} - 2Z_{p1}}{Z_{in1e} + 2Z_{p1}}\right|^2} \tag{15}$$

$$S_{23} = \frac{S_{22}^e - S_{22}^o}{2} = \frac{1}{2}\left(\left|\frac{Z_{in2e} - Z_{p2}}{Z_{in2e} + Z_{p2}}\right| - \left|\frac{Z_{in2o} - Z_{p2}}{Z_{in2o} + Z_{p2}}\right|\right) \tag{16}$$

where Z_{p1} and Z_{p2} are the impedances of Port1 and Port2, respectively. Z_{in1e} is the input impedance from Port1 under

TABLE 2. Comparison of the FPD with the state-of-the-art.

Reference	[18]	[19]	[20]	[21]	[22]	This work
Center Frequency (GHz)	1.51	0.9	2.31	2.43/5.06	2.3/3.5	**3.12/3.87**
3-dB FBW (%)	56.5	2.4	17.7	38.3/18.8	9/7.1	**9.6/7.5**
Insertion Loss (dB)	6.8*	4.75	4.2	3.8/4.4	4.2/4.5	**4.35/4.52**
Return Loss (dB)	>15	N/A	>20	>14.3/19.8	>17.6/21.4	**>21/14**
Lower Passband Roll-Off (dB/GHz)	230/223**	185/125**	77/65**	55/42**	57/124**	**51/238**
Upper Passband Roll-Off (dB/GHz)	N/A	N/A	N/A	38/48**	68/88**	**173/65**
In-band Isolation (dB)	>13	>23	>17	>24/20	>19.2/18.6	**>18.7/22.5**
Stopband Bandwidth	Up to 4.15 GHz	Up to 20 GHz	Up to 20 GHz	Up to 9.43 GHz	Up to 13.8 GHz	**Up to 40 GHz**
Rejection Level (dB)	>15	>20	>30	>16	>20	**>28**
Isolation Bandwidth	N/A	N/A	DC to 20 GHz	DC to 8.9 GHz	N/A	**DC to 36 GHz**
Stopband Isolation Level (dB)	N/A	N/A	>28	>18	N/A	**>28**
Size ($\lambda_g \times \lambda_g$)	0.32×0.32	0.1×0.2	0.555×0.689	0.67×0.68	N/A	**0.423×0.564**

*Four way filtering power divider.
**Calculated from the measured results.

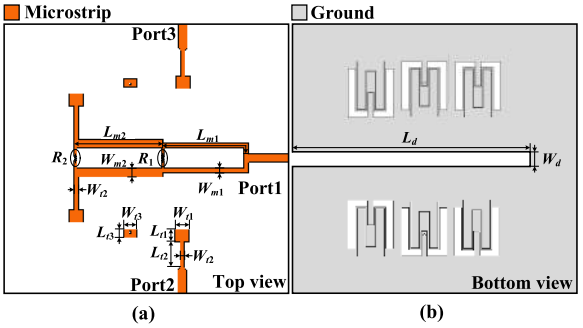

FIGURE 19. Configurations of the dual-band FPD. (a) Top view. (b) Bottom view.

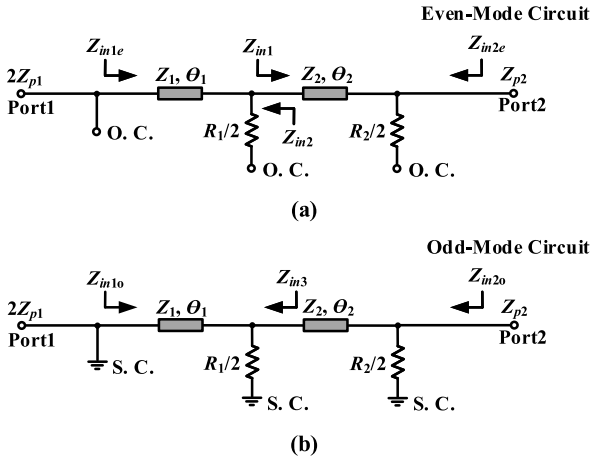

FIGURE 20. (a) Simplified even-mode equivalent circuit of the power divider part. (b) Simplified odd-mode equivalent circuit of the power divider part(o. c.: open circuit; s. c.: short circuit).

even-mode excitation, which could derive the return-loss (i.e., $|S_{11}|$) and insertion-loss (i.e., $|S_{21}|$ and $|S_{31}|$). Then, the output-isolation parameter (i.e., $|S_{23}|$) is determined by the input impedance for Port2 under the even-mode and odd-mode excitation (i.e., Z_{in2e} and Z_{in2o}). Note that,

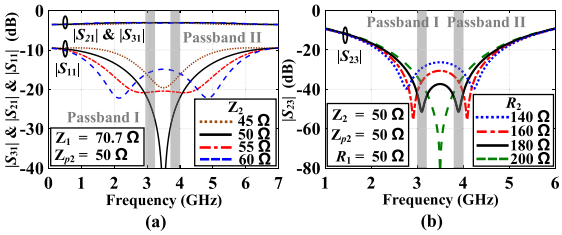

FIGURE 21. (a) Calculated power transmission ($|S_{21}|$ and $|S_{31}|$), input-reflection ($|S_{11}|$) with different Z_2 ($L_{m1} = L_{m2} = 15.67$ mm, and $W_{m1} = 0.87$ mm). (b) Calculated output-isolation ($|S_{23}|$) responses with different R_2 ($W_{m2} = 1.54$ mm).

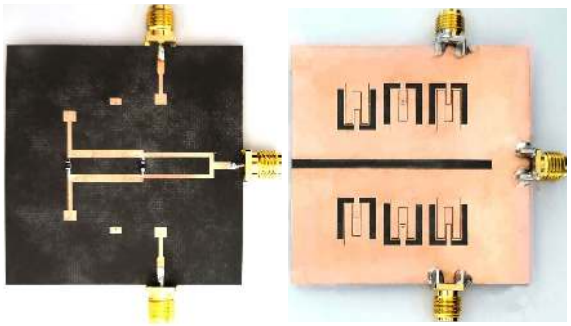

FIGURE 22. Photographs of the developed FPD prototype. (a) Top view. (b) Bottom view.

the expressions of Z_{in1e}, Z_{in2e}, and Z_{in2o} are shown in Appendix D.

The calculated $|S_{23}|$ by provided formulas with sweeping parameters of resistors is used to select the proper values. With various values of Z_2, the calculated curves associated to the $|S_{11}|$, $|S_{21}|$, and $|S_{31}|$ are shown in Fig. 21(a). Meanwhile, Fig. 21(b) depicts the calculated output-isolation parameters with different resistances (i.e., R_2). Here, two operation bands of filtering part are designed at 2.97–3.27 GHz and 3.72–4 GHz. Therefore, the characteristic impedance of Z_2

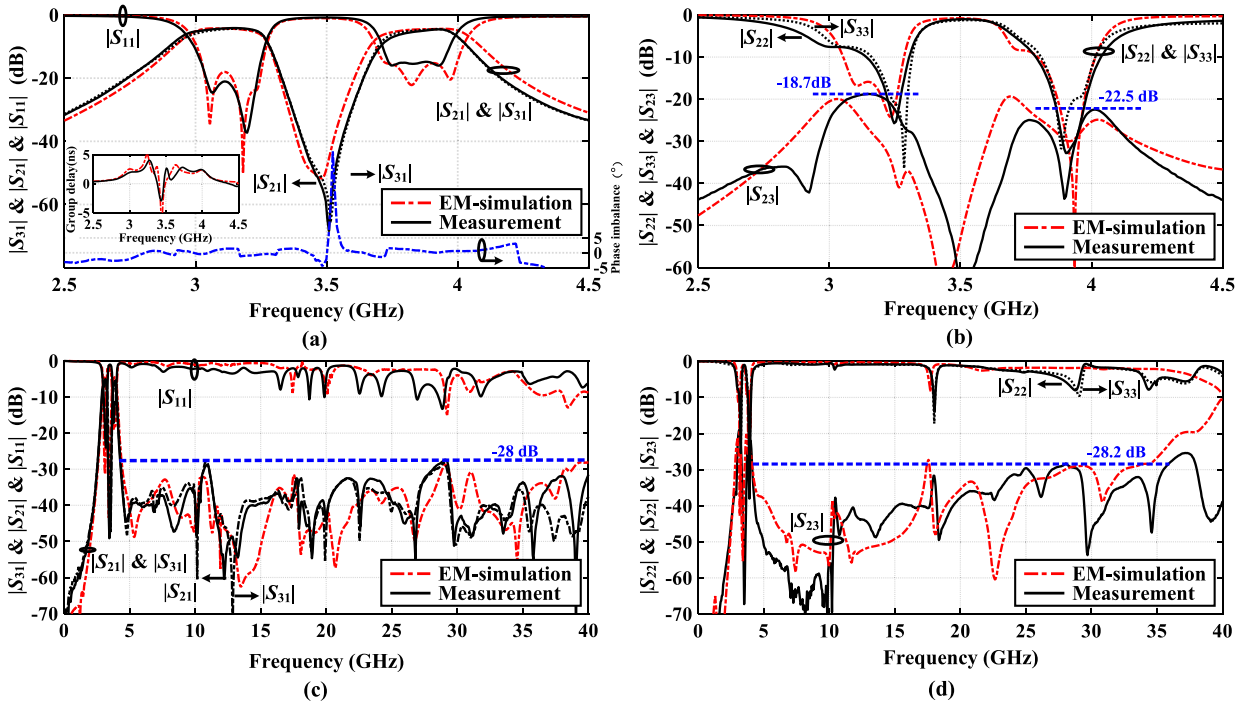

FIGURE 23. EM-simulated and measured power transmission ($|S_{21}|$ and $|S_{31}|$), input-reflection ($|S_{11}|$, $|S_{22}|$, and $|S_{33}|$), output-isolation ($|S_{23}|$), and group delay of the developed FPD prototype (the dimensions of the filter part are shown in Fig. 18, $L_{m1} = L_{m2} = 15.67$ mm, $W_{m1} = 0.87$ mm, $W_{m2} = 1.54$ mm, $W_d = 2$ mm, $L_d = 42$ mm, $R_1 = 50\ \Omega$, and $R_2 = 180\ \Omega$).

is selected as 50 Ω for a good in-band impedance matching. Besides, to achieve a high in-band isolation, the two transmission zeros for S_{23} are optimized at the center frequencies of these two operational bands. In this case, the R_1 and R_2 are chosen as 50 Ω and 180 Ω, respectively. Thus, the dual-band power divider could achieve the low insertion loss and high output isolation, simultaneously.

Then, based on the proposed hybrid microstrip/DGS cells, a dual-band FPD with ultra-wide upper stopband and output isolation is implemented and fabricated, as shown in Fig. 22. As depicted in Fig. 23, a good agreement between the EM-simulated and measured results is achieved. The measured dual-band FPD exhibits the dual-band with the center frequencies of 3.12 and 3.87 GHz, 3-dB FBWs of 9.6% and 7.5%, minimum in-band insertion loss of 4.35 and 4.52 dB (i.e., 1.35 dB and 1.52 dB excluding the loss with regard to the ideal 3-dB power-splitting factor), and minimum in-band isolation of 18.7 dB and 22.5 dB, respectively. Note that, the FPD can also achieve a minimum 28-dB out-of-band rejection up to 40 GHz. Besides, a high output isolation with a rejection level higher than 28 dB is measured up to 36 GHz. The constructed dual-band FPD features a compact core size of 33.94 mm × 38.3 mm (i.e., $0.423\lambda_g \times 0.564\lambda_g$, where λ_g is the microstrip guided wavelength on the substrate at the center frequency of the first passband). In Table 2, the performances of the proposed dual-band FPD are summarized and compared with the state-of-the arts FPDs [18]–[22]. In particular, the proposed FPD has merits of the sharp-rejection, dual-band operation, ultra-wide upper stopband, and high broad-band output isolation.

V. CONCLUSION

In this paper, two novel hybrid microstrip/DGS slow-wave cells with compact size and their applications are presented. Both cells can introduce dual-resonance with an ultra-wide stopband characteristic, due to the intrinsic slow-wave effect. Based on the hybrid microstrip/DGS cells, a series of dual-band BPFs and FPD has been proposed and fabricated. As demonstrated, such design examples have merits of the good in-band performance, ultra-wide stopband with high stopband rejection level, and closely-spaced passbands. Therefore, those performance advantages make the engineered BPF and FPD to be attractive for the practical application in modern multi-band RF front-ends.

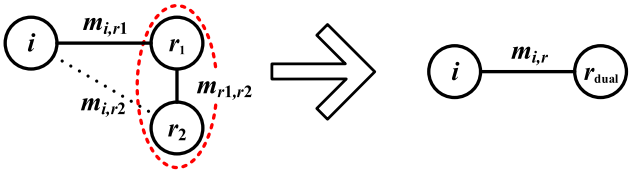

FIGURE 24. The coupling diagrams of the dual-resonance DGS when coupled with an arbitrary resonator.

APPENDIXES

APPENDIX A

Once an arbitrary resonator is coupled with the dual-resonance DGS, these two closely-coupled resonators could be considered as a whole resonant cell. As shown in Fig. 24, the resonator r_i acts as the arbitrary resonator, and the resonators r_1 and r_2 represent the stepped-impedance DGS and folded slotline, respectively. Then, the $m_{i,r1}$, $m_{i,r2}$, $m_{r1,r2}$ are

the coupling coefficients for these resonators, respectively. As shown in Fig. 2, the folded slotline is closely surrounded by the stepped-impedance DGS with folded design. In this case, the stepped-impedance DGS can not only introduce strong coupling with the folded slotline, but also cut off the couplings between slotline and other resonators. With such implementation, the proposed structure can be regarded as a dual-resonance DGS cell with a peninsula topology. In other words, the $m_{i,r1} \gg m_{i,r2}$. If the two single-mode resonators have resonant frequencies at ω_a and ω_b, respectively. Then, their transformed frequencies can be calculated as:

$$\Omega_{a(\omega)} = \gamma_a \frac{\omega^2 - \omega_a^2}{\omega\omega_a} \tag{17}$$

where the γ_a and γ_b are the parameters that define the transformations of the two resonators, respectively. Then, these two closely-coupled resonators can be considered as a dual-mode resonant cell [27], and thus, the transformed frequencies can be expressed as:

$$\begin{aligned}\Omega_{dual(\omega)} &= \frac{\Omega_{a(\omega)}\Omega_{b(\omega)} - m_{r1,r2}^2}{\Omega_{b(\omega)}} \\ &= \frac{\gamma_a\gamma_b(\omega^2 - \omega_a^2)(\omega^2 - \omega_b^2) - m_{r1,r2}^2\omega_a\omega_b\omega^2}{\gamma_b\omega\omega_a(\omega^2 - \omega_b^2)} \\ &= \gamma \frac{(\omega^2 - \omega_1^2)(\omega^2 - \omega_2^2)}{\omega\omega_a(\omega^2 - \omega_b^2)}\end{aligned} \tag{18}$$

where

$$\gamma = \gamma_a \tag{19}$$

$$\omega_1^2 + \omega_2^2 = \omega_a^2 + \omega_b^2 + \frac{m_{r1,r2}^2\omega_a\omega_b}{\gamma_a\gamma_b} \tag{20}$$

$$\omega_1^2\omega_2^2 = \omega_a^2\omega_b^2. \tag{21}$$

Note that, the ω_1 and ω_2 are the lower and higher resonant frequencies of the dual-resonance resonant cell, respectively. As proved in the equation (19), such dual-resonance resonator can also provide a transmission zero (i.e., ω_b) between the dual-resonance. Furthermore, the $m_{i,r}$ can be derived as

$$m_{i,r} \approx m_{i,r1}. \tag{22}$$

APPENDIX B

The expressions of slotline for low ϵ_r substrates are studied in [39] by curve fitting the numerical results. For $0.0015 \le W/\lambda_0 \le 0.075$ and $2.22 \le \epsilon_r \le 3.8$, the characteristic impedance of slotline can be derived as

$$\begin{aligned}Z_0 = {} & 60 + 3.69\sin[\frac{(\epsilon_r - 2.2)\pi}{2.36}] + 133.5\ln(10\epsilon_r)\sqrt{\frac{W}{\lambda_0}} \\ & +2.81[1 - 0.011\epsilon_r(4.48 - \ln\epsilon_r)](\frac{W}{h})\ln(\frac{100h}{\lambda_0}) \\ & +131.1(1.028 - \ln\epsilon_r)\sqrt{\frac{h}{\lambda_0}} \\ & +12.48\frac{(1 + 0.18\ln\epsilon_r)\frac{W}{h}}{\sqrt{\epsilon_r - 2.06 + 0.85(\frac{W}{h})^2}}.\end{aligned} \tag{23}$$

where c is the speed of light in vacuum, W is the width of slotline, λ_0 is the guided wavelength in vacuum, ϵ_r is the dielectric constant, and h is the thickness of the dielectric substrate, respectively. Assuming the length of the slotline is L_s, the θ_l can be calculated as

$$\theta_l = \beta\frac{L_s}{2} = \frac{\pi f_0 L_s}{c(A - B\ln\frac{f_0 h}{c})} \tag{24}$$

where

$$A = 1.045 - 0.365\ln\epsilon_r + \frac{6.3\left(\frac{W}{h}\right)\epsilon_r^{0.945}}{238.64 + 100\left(\frac{W}{h}\right)} \tag{25}$$

$$B = 0.148 - \frac{8.81\,(\epsilon_r + 0.95)}{100\epsilon_r}. \tag{26}$$

APPENDIX C

The symmetry and asymmetry dual-band BPFs with the topology (i.e., as shown in Fig. 14(a)) can be determined by ω_{L1}, ω_{L2}, ω_{H1}, and ω_{H2}, according to [26] and [36]. Here, the ω_{L1} and ω_{H1} define the lower passband, while the ω_{L2} and ω_{H2} determine the upper one. These passbands are separated by means of an inter-band transmission zero at ω_z. Then, the frequencies ω_a and ω_b, parameters γ_a and γ_b, and k_{cell} can be derived as follow:

$$\omega_a = \sqrt{\frac{\omega_{L1}\omega_{L2}\omega_{H1}\omega_{H2}\left[(\omega_{H1} + \omega_{H2}) - (\omega_{L1} + \omega_{L2})\right]}{\omega_{H1}\omega_{H2}\left(\omega_{L1} + \omega_{L2}\right) - \omega_{L1}\omega_{L2}\left(\omega_{H1} + \omega_{H2}\right)}} \tag{27}$$

$$\omega_b = \sqrt{\frac{\omega_{H1}\omega_{H2}(\omega_{L1} + \omega_{L2}) - \omega_{L1}\omega_{L2}(\omega_{H1} + \omega_{H2})}{(\omega_{H1} + \omega_{H2}) - (\omega_{L1} + \omega_{L2})}} \tag{28}$$

$$\gamma_a = \frac{\omega_a}{(\omega_{H1} + \omega_{H2}) - (\omega_{L1} + \omega_{L2})} \tag{29}$$

$$\gamma_b = \frac{[(\omega_{H1} + \omega_{H2}) - (\omega_{L1} + \omega_{L2})]\omega_b}{C - \omega_a^2 - \omega_b^2} \tag{30}$$

$$k_{cell} = \sqrt{\frac{C - \omega_a^2 - \omega_b^2}{\omega_a\omega_b}} \tag{31}$$

where

$$C = (\omega_{H1} + \omega_{H2})\,(\omega_{L1} + \omega_{L2}) - \omega_{H1}\omega_{H2} - \omega_{L1}\omega_{L2}. \tag{32}$$

where k_{cell} is the coupling coefficient between two resonators in cells, the γ_a and γ_b are the parameters that define the transformations of these two resonators, and the parameters ω_a and ω_b are resonant frequencies of these two resonators in the absence of coupling.

APPENDIX D

As shown in [40], the input impedance parameters of the equivalent circuit model in Fig. 20 can be expressed as:

$$Z_{in1e} = Z_1 \frac{Z_{in1} + jZ_1 \tan\theta_1}{Z_1 + jZ_{in1} \tan\theta_1} \tag{33}$$

$$Z_{in2e} = Z_2 \frac{Z_{in2} + jZ_2 \tan\theta_2}{Z_2 + jZ_{in2} \tan\theta_2} \tag{34}$$

$$Z_{in2o} = \frac{Z_2 Z_{in3} R_2 + jZ_2^2 R_2 \tan\theta_2}{R_2 Z_2 + 2Z_2 Z_{in3} + j \tan\theta_2 \left(R_2 Z_{in3} + 2Z_2^2\right)} \tag{35}$$

where

$$Z_{in1} = Z_2 \frac{Z_{p2} + jZ_2 \tan\theta_2}{Z_2 + jZ_{p2} \tan\theta_2} \tag{36}$$

$$Z_{in2} = Z_1 \frac{2Z_{p1} + jZ_1 \tan\theta_1}{Z_1 + 2jZ_{p1} \tan\theta_1} \tag{37}$$

$$Z_{in3} = \frac{R_1 Z_1 \left(2Z_{p1} + jZ_1 \tan\theta_1\right)}{R_1 Z_1 + 4Z_1 Z_{p1} + j \tan\theta_1 \left(2R_1 Z_{p1} + Z_1^2\right)}. \tag{38}$$

REFERENCES

[1] L. Han and K. Wu, "Multifunctional transceiver for future intelligent transportation systems," *IEEE Trans. Microw. Theory Techn.*, vol. 59, no. 7, pp. 1879–1892, Jul. 2011.
[2] M. Brandolini, P. Rossi, D. Manstretta, and F. Svelto, "Toward multistandard mobile terminals–fully integrated receivers requirements and architectures," *IEEE Trans. Microw. Theory Techn.*, vol. 53, no. 3, pp. 1026–1038, Mar. 2005.
[3] L. Zhu, S. Sun, and W. Menzel, "Ultra-wideband (UWB) bandpass filters using multiple-mode resonator," *IEEE Microw. Wireless Compon. Lett.*, vol. 15, no. 11, pp. 796–798, Nov. 2005.
[4] B. Archambeault, C. Brench, and S. Connor, "Review of printed-circuit-board level EMI/EMC issues and tools," *IEEE Trans. Electromagn. Compat.*, vol. 52, no. 2, pp. 455–461, May 2010.
[5] B. Mohajer-Iravani, S. Shahparnia, and O. Ramahi, "Coupling reduction in enclosures and cavities using electromagnetic band gap structures," *IEEE Trans. Electromagn. Compat.*, vol. 48, no. 2, pp. 292–303, May 2006.
[6] M. Velazquez-Ahumada, J. Martel, and F. Medina, "Parallel coupled microstrip filters with floating ground-plane conductor for spurious-band suppression," *IEEE Trans. Microw. Theory Techn.*, vol. 53, no. 5, pp. 1823–1828, May 2005.
[7] T. Lopetegi, M. Laso, J. Hernandez, M. Bacaicoa, D. Benito, M. Garde, M. Sorolla, and M. Guglielmi, "New microstrip 'Wiggly-Line' filters with spurious passband suppression," *IEEE Trans. Microw. Theory Techn.*, vol. 49, no. 9, pp. 1593–1598, Sep. 2001.
[8] J.-T. Kuo, W.-H. Hsu, and W.-T. Huang, "Parallel coupled microstrip filters with suppression of harmonic response," *IEEE Microw. Wireless Compon. Lett.*, vol. 12, no. 10, pp. 383–385, Oct. 2002.
[9] J.-S. Park, J.-S. Yun, and D. Ahn, "A design of the novel coupled-line bandpass filter using defected ground structure with wide stop-band performance," *IEEE Trans. Microw. Theory Techn.*, vol. 50, no. 9, pp. 2037–2043, Sep. 2002.
[10] P. Cheong, S.-W. Fok, and K.-W. Tam, "Miniaturized parallel coupled-line bandpass filter with spurious-response suppression," *IEEE Trans. Microw. Theory Techn.*, vol. 53, no. 5, pp. 1810–1816, May 2005.
[11] J.-K. Lee and Y.-S. Kim, "Ultra-wideband bandpass filter with improved upper stopband performance using defected ground structure," *IEEE Microw. Wireless Compon. Lett.*, vol. 20, no. 6, pp. 316–318, Jun. 2010.
[12] C.-F. Chen, T.-Y. Huang, and R.-B. Wu, "Design of microstrip bandpass filters with multiorder spurious-mode suppression," *IEEE Trans. Microw. Theory Techn.*, vol. 53, no. 12, pp. 3788–3793, Dec. 2005.
[13] X. Luo, J.-G. Ma, E.-P. Li, and K. Ma, "Hybrid microstrip T-stub/defected ground structure cell for electromagnetic interference bandpass filter design," *IEEE Trans. Electromagn. Compat.*, vol. 53, no. 3, pp. 717–725, Aug. 2011.
[14] H. H. Ta and A.-V. Pham, "Dual band band-pass filter with wide stopband on multilayer organic substrate," *IEEE Microw. Wireless Compon. Lett.*, vol. 23, no. 4, pp. 193–195, Apr. 2013.
[15] C. H. Kim and K. Chang, "Independently controllable dual-band band-pass filters using asymmetric stepped-impedance resonators," *IEEE Trans. Microw. Theory Techn.*, vol. 59, no. 12, pp. 3037–3047, Dec. 2011.
[16] J.-T. Kuo and H.-P. Lin, "Dual-band bandpass filter with improved performance in extended upper rejection band," *IEEE Trans. Microw. Theory Techn.*, vol. 57, no. 4, pp. 824–829, Apr. 2009.
[17] C.-H. Tseng and H.-Y. Shao, "A new dual-band microstrip bandpass filter using net-type resonators," *IEEE Microw. Wireless Compon. Lett.*, vol. 20, no. 4, pp. 196–198, Apr. 2010.
[18] H. Zhu, A. M. Abbosh, and L. Guo, "Wideband four-way filtering power divider with sharp selectivity and wide stopband using looped coupled-line structures," *IEEE Microw. Wireless Compon. Lett.*, vol. 26, no. 6, pp. 413–415, Jun. 2016.
[19] W.-M. Chau, K.-W. Hsu, and W.-H. Tu, "Filter-based Wilkinson power divider," *IEEE Microw. Wireless Compon. Lett.*, vol. 24, no. 4, pp. 239–241, Apr. 2014.
[20] L. Fan, H. J. Qian, B. Yangl, G. Wang, and X. Luo, "Filtering power divider with wide stopband using open-stub loaded coupled-line and hybrid microstrip T-stub/DGS cell," in *IEEE MTT-S Int. Microw. Symp. Dig.*, Jun. 2018, pp. 1–4.
[21] X. Wang, J. Wang, W.-W. Choi, L. Yang, and W. Wu, "Dual-wideband filtering power divider based on coupled stepped-impedance resonators," *IEEE Microw. Wireless Compon. Lett.*, vol. 28, no. 10, pp. 873–875, Oct. 2018.
[22] P. Wen, Z. Ma, H. Liu, S. Zhu, B. Ren, Y. Song, X. Wang, and M. Ohira, "Dual-band filtering power divider using dual-resonance resonators with ultrawide stopband and good isolation," *IEEE Microw. Wireless Compon. Lett.*, vol. 29, no. 2, pp. 101–103, Feb. 2019.
[23] S. Avrillon, I. Pele, A. Chousseaud, and S. Toutain, "Dual-band power divider based on semiloop stepped-impedance resonators," *IEEE Trans. Microw. Theory Techn.*, vol. 51, no. 4, pp. 1269–1273, Apr. 2003.
[24] H. Oraizi and M. S. Esfahlan, "Miniaturization of Wilkinson power dividers by using defected ground structures," *Prog. Electromagn. Res. Lett.*, vol. 4, pp. 113–120, 2008.
[25] Y. Rao, H. J. Qian, R. Gomez-Garcia, and X. Luo, "Dual-band bandpass filter with ultra-wide upper stopband using slow-wave dual-resonance cells," in *IEEE MTT-S Int. Microw. Symp. Dig.*, Jun. 2018, pp. 537–539.
[26] G. Macchiarella and S. Tamiazzo, "Design techniques for dual-passband filters," *IEEE Trans. Microw. Theory Techn.*, vol. 53, no. 11, pp. 3265–3271, Nov. 2005.
[27] P. Ma, B. Wei, J. Hong, X. Guo, B. Cao, and L. Jiang, "Coupling matrix compression technique for high-isolation dual-mode dual-band filters," *IEEE Trans. Microw. Theory Techn.*, vol. 66, no. 6, pp. 2814–2821, Jun. 2018.
[28] D. Ahn, J. S. Park, C. S. Kim, J. Kim, Y. Qian, and T. Itoh, "A design of the low-pass filter using the novel microstrip defected ground structure," *IEEE Trans. Microw. Theory Techn.*, vol. 49, no. 1, pp. 86–93, Jan. 2001.
[29] J.-S. Hong, *Microstrip Filters for RF/Microwave Applications*, 2nd ed. New York, NY, USA: Wiley, 2011.
[30] A. Boutejdar, A. Batmanov, A. Omar, and E. Burte, "A miniature 3.1 GHz microstrip bandpass filter with suppression of spurious harmonics using multilayer technique and defected ground structure open-loop ring," in *Ultra-Wideband, Short Pulse Electromagnetics 9*. New York, NY, USA: Springer-Verlag, May 2010, pp. 185–191.
[31] Q. Xue, K. M. Shum, and C. H. Chan, "Novel 1-D microstrip PBG cells," *IEEE Microw. Guided Wave Lett.*, vol. 10, no. 10, pp. 403–405, Oct. 2000.
[32] J.-S. Hong and M. Lancaster, "Theory and experiment of novel microstrip slow-wave open-loop resonator filters," *IEEE Trans. Microw. Theory Techn.*, vol. 45, no. 12, pp. 2358–2365, Dec. 1997.
[33] I. J. Bahl, M. Bozzi, and R. Garg, *Microstrip Lines and Slotlines*, 3rd ed. Boston, MA, USA: Artech House, 2013.
[34] S. V. Robertson and L. P. B. Katehi, "A planar quasi-optical mixer using a folded-slot antenna," *IEEE Trans. Microw. Theory Techn.*, vol. 43, no. 4, pp. 896–898, Apr. 1995.
[35] J. B. Knorr and J. Saenz, "End effect in a shorted slot," *IEEE Trans. Microw. Theory Techn.*, vol. MTT-21, no. 9, pp. 579–580, Sep. 1973.
[36] A. Garcia-Lamperez and M. Salazar-Palma, "Single-band to multiband frequency transformation for multiband filters," *IEEE Trans. Microw. Theory Techn.*, vol. 59, no. 12, pp. 3048–3058, Dec. 2011.
[37] X. Luo, B. Yang, and H. J. Qian, "Adaptive synthesis for resonator-coupled filters based on particle swarm optimization," *IEEE Trans. Microw. Theory Techn.*, vol. 67, no. 2, pp. 712–725, Feb. 2019.
[38] S. Cohn, "A class of broadband three-port TEM-mode hybrids," *IEEE Trans. Microw. Theory Techn.*, vol. MTT-16, no. 2, pp. 110–116, Feb. 1968.

[39] R. Janaswamy and D. Schaubert, "Characteristic impedance of a wide slotline on low-permittivity substrates (short paper)," *IEEE Trans. Microw. Theory Techn.*, vol. MTT-34, no. 8, pp. 900–902, Aug. 1986.
[40] D. M. Pozar, *Microwave Engineering*, 4th ed. New, York, NY, USA: Wiley, 2012.

YUNBO RAO (Student Member, IEEE) received the B.E. degree in microelectronics from the University of Electronic Science and Technology of China, Chengdu, China, in 2017, where he is currently pursuing the Ph.D. degree in microelectronics and solid-state electronics. His current research interests include microwave and millimeter-wave passive components. He was a recipient of the IEEE IMS Student Design Competition Award (First Place), in 2019.

HUIZHEN JENNY QIAN (Member, IEEE) received the B.E., M.Sc., and Ph.D. degrees in electronic engineering from the University of Electronic Science and Technology of China (UESTC), Chengdu, China, in 2008, 2011, and 2018, respectively.

Since 2019, she has been an Assistant Professor with the Center for Integrated Circuits, UESTC. Her research interests include the wideband microwave/millimeter-wave transceivers, reconfigurable passive circuits, and on-chip array systems.

Dr. Qian is a Technical Program Committee Member of the IEEE International Wireless Symposium (IWS). She also serves as a Reviewer for several IEEE journals, including the IEEE TRANSACTIONS ON MICROWAVE THEORY AND TECHNIQUES and the IEEE TRANSACTIONS ON CIRCUITS AND SYSTEMS–I: REGULAR PAPERS. She was a recipient or a co-recipient of the 2018 IEEE MTT-Society Graduate Fellowship Award, the IEEE IWS Best Student Paper Award, in 2015 and 2018, the IEEE IMS Student Design Competition Award, in 2017 and 2018, and the IEEE RFIT Best Student Paper Award, in 2016 and 2019.

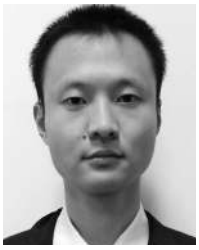

BINGZHENG YANG (Student Member, IEEE) received the B.E. degree in microelectronics from the University of Electronic Science and Technology of China, Chengdu, China, in 2016, where he is currently pursuing the Ph.D. degree in microelectronics and solid-state electronics.

His current research interests include microwave transmitter and passive components, especially for integrated circuits.

ROBERTO GÓMEZ-GARCÍA (Senior Member, IEEE) received the M.Sc. degree in telecommunication engineering and the Ph.D. degree in electrical and electronic engineering from the Polytechnic University of Madrid, Madrid, in 2001 and 2006, respectively.

Since 2006, he has been an Associate Professor with the Department of Signal Theory and Communications, University of Alcalá, Madrid. He has been, for several research stays, with the University of Limoges, University of Aveiro, U.S. Naval Research Laboratory, and Purdue University. He was an invited Visiting Professor at the Gdansk University of Technology, Gdansk, Poland, from 2018 to 2019. He is currently a part-time Adjunct Professor with the University of Electronic Science and Technology of China, Chengdu, China. His current research interests include the design of fixed/tunable high-frequency filters and multiplexers in planar, hybrid, and monolithic microwave-integrated circuit technologies, multifunction circuits and systems, and software-defined radio and radar architectures for telecommunications, remote sensing, and biomedical applications, in which he has authored or coauthored around 90 journal articles and 135 conference papers.

Dr. Gómez-García serves as a member of the Technical Review Board for several IEEE and EuMA conferences. He is also a Technical Committee member of MTT-5 on Filters, MTT-6 on RF MEMs and Microwave Acoustics, MTT-23 on Wireless Communications, and MTT-28 on Biological Effects and Medical Applications. He was a recipient of the 2016 IEEE Microwave Theory and Techniques Society Outstanding Young Engineer Award. He was an Associate Editor of the IEEE TRANSACTIONS ON MICROWAVE THEORY AND TECHNIQUES, from 2012 to 2016, and the IEEE TRANSACTIONS ON CIRCUITS AND SYSTEMS–I: REGULAR PAPERS, from 2012 to 2015. He is currently an Associate Editor of the IEEE JOURNAL OF ELECTROMAGNETICS, RF AND MICROWAVES IN MEDICINE AND BIOLOGY, IEEE ACCESS, the *IET Microwaves, Antennas & Propagation*, and the *International Journal of Microwave and Wireless Technologies*.

XUN LUO (Senior Member, IEEE) received the B.E. and Ph.D. degrees in electronic engineering from the University of Electronic Science and Technology of China (UESTC), Chengdu, China, in 2005 and 2011, respectively.

From 2010 to 2013, he was with Huawei Technologies Company, Ltd., Shenzhen, China, as a Project Manager, to guide research and development projects of multiband microwave/mm-wave integrated systems for backhaul and wireless communication. Since 2015, he has been with UESTC, as a Full Professor, and appointed as the Executive Director of the Center for Integrated Circuits. Before joining UESTC, he was an Assistant Professor with the Department of Microelectronics, Delft University of Technology, Delft, The Netherlands. He has authored or coauthored over 80 journal and conference papers. He holds 23 patents in the area of wireless application. His current research interests include RF/microwave/mm-wave integrated circuits, multiple-resonance THz modules, reconfigurable passive circuits, smart antennas with sensor networks, artificial-intelligence microsystems, multifunction backhaul/wireless application, and system in package.

Dr. Luo is a Technical Program Committee Member of the IEEE International Microwave Symposium (IMS), the IEEE Radio Frequency Integrated Circuits Symposium (RFIC), and the IEEE International Wireless Symposium (IWS). He is also a Technical Committee Member of MTT-5 on Filters and MTT-23 on Wireless Communications. He was bestowed by the Recruitment Program of Global Experts Award, China, in 2015, and the China Overseas Chinese Contribution Award, in 2016. He was also a recipient of the UESTC Distinguished Innovation and Teaching Award, in 2018, and the UESTC Outstanding Undergraduate Teaching Promotion Award, in 2016. His research group BEAM X-Lab received multiple Best Paper Awards and Best Design Competition Awards, including the IEEE IWS Best Student Paper Award, in 2015 and 2018, the IEEE RFIT Best Student Paper Award, in 2016 and 2019, the IEEE IMS Best Student Design Competition Award, from 2017 to 2019, the IEEE IMS Sixty-Second Presentation Competition Award, in 2019, and multiple Best Paper Award finalists of the IEEE conferences. He was the TPC Co-Chair of the IEEE IWS, in 2018 and the IEEE RFIT, in 2019. He serves as a Track Editor of the IEEE MICROWAVE AND WIRELESS COMPONENTS LETTERS and is also an Associate Editor of the *IET Microwaves, Antennas & Propagation*.